Dust beyond the torus: revealing the mid-infrared heart of local Seyfert ESO 428-G14 with *JWST*/MIRI

Houda Haidar [1]*, David J. Rosario,[1] Almudena Alonso-Herrero,[2] Miguel Pereira-Santaella,[3]
Ismael García-Bernete,[4] Stephanie Campbell [1], Sebastian F. Hönig,[5] Cristina Ramos Almeida [6,7]
Erin Hicks,[8,9,10] Daniel Delaney,[8,9] Richard Davies [11], Claudio Ricci,[12,13] Chris M. Harrison [1],
Mason Leist,[10] Enrique Lopez-Rodriguez [14] Santiago Garcia-Burillo,[15] Lulu Zhang [10],
Chris Packham,[10,16] Poshak Gandhi [5], Anelise Audibert,[6,7] Enrica Bellocchi [17,18] Peter Boorman,[19,20]
Andrew Bunker,[4] Françoise Combes,[21] Tanio Diaz Santos,[22,23] Fergus R. Donnan [4],
Omaira Gonzalez Martin,[24] Laura Hermosa Muñoz,[2] Matthaios Charidis,[1] Alvaro Labiano,[25]
Nancy A. Levenson,[26] Daniel May,[27] Dimitra Rigopoulou [4,28] Alberto Rodriguez Ardila [29,30]
T. Taro Shimizu [11] Marko Stalevski [31,32] and Martin Ward[33]

Affiliations are listed at the end of the paper

ABSTRACT

Polar dust has been discovered in a number of local active galactic nuclei (AGN), with radiation-driven torus models predicting a wind to be its main driver. However, little is known about its characteristics, spatial extent, or connection to the larger scale outflows. We present the first *JWST*/MIRI study aimed at imaging polar dust by zooming on to the centre of ESO 428-G14, part of the Galaxy Activity, Torus, and Outflow Survey (GATOS) survey of local AGN. We detect extended mid-infrared (MIR) emission within 200 pc from the nucleus. This polar structure is co-linear with a radio jet and lies perpendicular to a molecular gas lane that feeds and obscures the nucleus. Its morphology bears a striking resemblance to that of gas ionized by the AGN in the narrow-line region. We demonstrate that part of this spatial correspondence is due to contamination within the *JWST* filter bands from strong emission lines. Correcting for the contamination, we find the morphology of the dust continuum to be more compact, though still clearly extended out to $r \approx 100$ pc. We estimate the emitting dust has a temperature of ~ 120 K. Using simple models, we find that the heating of small dust grains by the radiation from the central AGN and/or radiative jet-induced shocks is responsible for the extended MIR emission. Radiation-driven dusty winds from the torus is unlikely to be important. This has important implications for scales to which AGN winds can carry dust and dense gas out into their host galaxies.

Key words: methods: observational – galaxies: active – galaxies: nuclei – galaxies: Seyfert.

1 INTRODUCTION

For decades, the dusty torus has been held responsible for the dichotomy between type 1 and type 2 active galactic nuclei (AGN), forming the keystone of AGN unification (Antonucci & Miller 1985; Urry & Padovani 1995). Therefore, our insights into the AGN model and unification theory owe much to our ability to constrain the torus, and our understanding of dusty material in the vicinity of supermassive black holes (SMBHs). Pioneering observations with the Atacama Large Millimeter/submillimeter Array (ALMA) have, for the first time, enabled the detection and resolution of parsec-scale dusty molecular tori (~ 3 to 50 pc) first in NGC1068 and later on in some local AGN (Gallimore et al. 2016; García-Burillo et al. 2016, 2019, 2021; Alonso-Herrero et al. 2018, 2019, 2023; Combes et al. 2019). At the same time, images of the torus are now being

produced by the new generation of near- and mid-infrared (MIR) interferometers (GRAVITY Collaboration. 2020; Gámez Rosas et al. 2022).

The AGN-heated dust in the torus spans a range of temperatures from tens to ~ 1800 K, and peaks in the MIR range ($\lambda = 5$–30 µm). This makes observations in the MIR part of the spectrum crucial for revealing the characteristics and structure of the torus. MIR observations have uncovered unprecedented details about the circumnuclear dust distribution in local Seyfert galaxies (e.g. Jaffe et al. 2004; Tristram et al. 2007; Burtscher et al. 2009; Ramos Almeida et al. 2009, 2011; Reunanen et al. 2010; Alonso-Herrero et al. 2014, 2016; García-Bernete et al. 2015, 2016; González-Martín et al. 2019). In some Seyfert galaxies, interferometric and single-dish observations revealed the dust to be distributed in a two-component system, with the majority of its MIR emission emerging from the polar direction (e.g. Hönig et al. 2012, 2013; López-Gonzaga et al. 2014; Tristram et al. 2014; Leftley et al. 2018). Systematic

studies have shown that the polar dust can be traced from a few parsecs (e.g. López-Gonzaga et al. 2016; Leftley et al. 2018; Gámez Rosas et al. 2022; Isbell et al. 2022) to as far as a few hundred parsecs from the central engine (e.g. Radomski et al. 2003; Packham et al. 2005; Asmus et al. 2014, 2016; García-Bernete et al. 2016; Alonso-Herrero et al. 2021). However, the origin of the extended MIR emission (tens to hundreds of parsecs) is not clear yet, because it can include line emitting gas in the narrow line region (NLR), ambient dust in the NLR, and/or outflowing dust driven from the central region (Ramos Almeida & Ricci 2017; Hönig 2019).

Various torus models have been proposed to reproduce the infrared emission of AGN and to help constrain torus properties and dynamics (e.g. Krolik & Begelman 1988; Emmering et al. 1992; Nenkova et al. 2008; Hönig & Kishimoto 2010; González-Martín et al. 2023). The detection of polar emission motivated the inclusion of a polar component associated with dust driven by a wind, launched from the inner parts of the torus, and powered by radiation pressure (e.g. Hönig et al. 2012, 2013; Hönig & Kishimoto 2017). For instance, radiative transfer models that incorporate disc + wind components are able to reproduce the observed polar dust structures (e.g. Hönig & Kishimoto 2017; Stalevski et al. 2017, 2019). In agreement with this, modern hydrodynamical simulations that incorporate radiative feedback predict polar dust to be a common feature in AGN, subject to high Eddington ratios (e.g. Wada et al. 2016; Williamson et al. 2020). The detection of a clear decrease in the fraction of obscured AGN at $\lambda_{\rm Edd} \geq 10^{-2}$ further confirms the idea that radiation pressure on dust is fundamental in shaping the environments of AGN (Ricci et al. 2017). As such, a revised model of the obscuring torus has been put forward, where the torus is now described as a complex entity with multiple components and phases (e.g. Ramos Almeida & Ricci 2017; Izumi et al. 2018; Hönig 2019; Alonso-Herrero et al. 2021). However, even if the dust is not part of a dusty wind, it can still substantially contribute to obscuration if it is just dust in the NLR heated by the central engine (e.g. Radomski et al. 2003).

Earlier ground-based work has reported that the silicate emission feature around 10 μm is absent in the polar dust (e.g. Hönig et al. 2012, 2013; Burtscher et al. 2013). This is best explained by the sublimation of small silicate grains and/or a dusty wind predominantly composed of large graphite grains (Hönig et al. 2012) which do not produce silicate features (e.g. Laor & Draine 1993). A physical mechanism for the destruction of grains in a wind was proposed by Tazaki & Ichikawa (2020). In this model, dust grains entrained in the wind are subject to hypersonic drift due to radiation pressure, which ultimately destroys them by kinetic sputtering. Smaller grains are more rapidly destroyed than larger grains (Draine & Salpeter 1979), which results in only the larger grains surviving beyond the inner several parsecs (Tazaki & Ichikawa 2020).

While ground-based observations found compelling evidence of polar dust, they are still limited by observing conditions (e.g. high thermal background, unstable PSF) that make it difficult to resolve polar dust emissions, and even if detected, the polar structure can only be traced out to a few hundred parsecs (Asmus et al. 2016). In general, the challenge in detecting polar dust emissions lies not just in technical limitations but also in distinguishing these emissions from the surrounding galaxy, particularly for weaker AGN (González-Martín et al. 2015, 2017). With the launch of the *JWST* (Gardner et al. 2023), offering unparalleled resolution and sensitivity, we can now image and trace the extent of polar dust emission from a parsec and a kiloparsec scale.

With this aim, we present a multiband imaging study of ESO 428-G14 with the MIRI instrument (Rieke et al. 2015; Wright et al. 2015, 2023) covering a wavelength range from 5.6 to 21 μm. ESO 428-G14

was selected as it shows prior evidence of polar MIR emission from ground-based observations (Asmus et al. 2016). By combining our new MIRI data with the wealth and variety of ancillary photometry already available for ESO 428-G14, we are able to explore in great detail the nature of its MIR emission, but also to place it within the broader context of this AGN.

1.1 ESO 428-G14

ESO 428-G14 is a spiral galaxy (see Fig. 1) with a redshift-independent distance of $D \approx 23.2$ Mpc (a projected physical scale of ≈ 112.5 pc per arcsecond) and a redshift of $z = 0.0057$ (values extracted from NED). It is classified optically as a Seyfert 2 galaxy (Véron-Cetty & Véron 2006), is Compton-thick in X-rays (Maiolino et al. 1998), and has an intrinsic 2–10 keV luminosity $L_{\rm AGN} = 3.6 \times 10^{41}$ ergs^{-1} (Levenson et al. 2006), and an estimated BH mass of $M_{\rm BH} \sim (1 - -3) \times 10^7$ M$_\odot$ (Fabbiano et al. 2019).

Observations by Ulvestad & Wilson (1989) uncovered a bent radio jet elongated along the galaxy's major axis. Hubble Space Telescope (HST) emission-line images revealed that the NLR is bi-polar and asymmetric, forming a rough double-helical shape to the North-West, and a larger elongated curved structure to the South-East, which appears to be co-spatial with the radio morphology (Falcke et al. 1996, 1998).

Analysis conducted by Riffel et al. (2006) using the Gemini Near-Infrared Spectrograph Integral Field Unit (GNIRS IFU) over the inner 300 pc found that the jet is launched with a slight inclination relative to the galactic plane. Riffel et al. (2006) also identified strong correlations between the flux and kinematics of various emission lines, notably the [Fe II]1.257 μm line, and the radio emission, suggesting that the radio jet is responsible in part for the observed outflows. This is further supported by spectral analysis on the central 4 arcsec × 4 arcsec region that favours the presence of shocks triggered by the interaction between the radio jet and the interstellar medium (ISM) in driving some of these outflows (May et al. 2018; Fabbiano et al. 2018a).

Recent ALMA CO (2-1) observations and modelling (Feruglio et al. 2020) revealed the presence of a bar or warped disc, potentially contributing to the Compton-thickness observed in X-rays (Fabbiano et al. 2017, 2018a, b). Additionally, Feruglio et al. (2020) detected a bi-polar molecular outflow along similar positional angle (PA) to the radio jet, and at distances ~ 700 pc from both sides of the nucleus. Feruglio et al. (2020) suggest potential interactions between the AGN wind and material in the galactic disc could lift up CO material from the galactic plane, leading to the observed CO outflow.

This paper is structured as follows. We describe the *JWST*/MIRI imaging observations and data reduction techniques in Section 2. Ancillary data used in this study are presented in Section 3. Our findings are detailed in Section 4, followed by a discussion in Section 5. Finally, we summarize our findings and conclusions in Section 6.

2 *JWST* OBSERVATIONS AND DATA REDUCTION

ESO 428-G14 is part of a sample of eight nearby Seyfert galaxies from the *JWST* Cycle 1 programme 'Dust in the Wind' (ID: 2064, PI: David Rosario) within the ambit of the *Galactic Activity, Torus, and Outflow Survey* (GATOS) collaboration (see also Alonso-Herrero et al. 2021; García-Burillo et al. 2021; García-Bernete et al. 2024).

On the 21$^{\rm st}$ of October, 2022, ESO 428-G14 was observed in five broad-band filters (*F560W*, *F1000W*, *F1500W*, *F1800W*, *F2100W*,
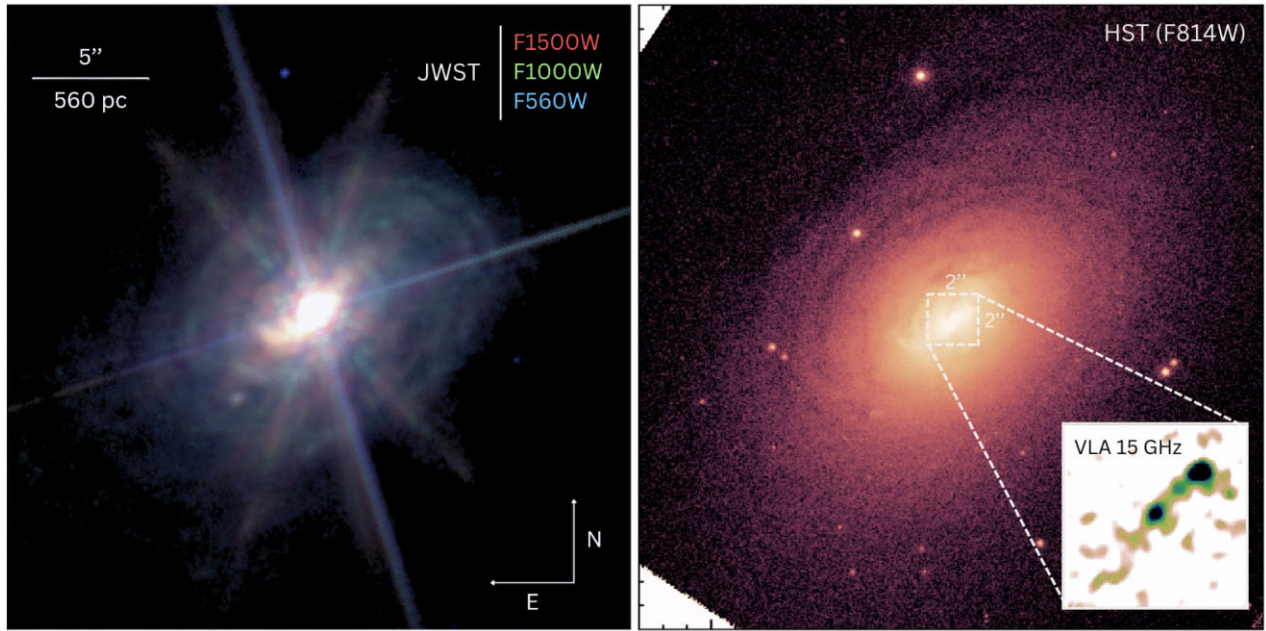
Figure 1. Left: RGB composite image of the *JWST*/MIRI images of ESO 428-G14, where red, green, and blue channels correspond to *F*1500*W*, F1000*W*, and *F*560*W* filters, respectively. The combination of these three filters reveals the MIR structure of the circumnuclear disc along with the small-scale nuclear extensions. The field of view (FOV) is ∼ 25″ across. The strong diffraction spikes are due to the bright central point-like source, which has not been subtracted in the version of the images used for this composite. Right: Optical HST image of ESO 428-G14 in the *F*814*W* filter over the same FOV as the *JWST* colour composite from the left-hand panel. Zooming into the inner 2 arcsec × 2 arcsec region, the radio jet traced by the VLA 15 GHz emission is displayed in the bottom right of the figure.

corresponding to $\lambda_{central}$ = 5.6, 10, 15, 18, and 21 μm, respectively). The SUB256 subarray was used (28″.2 on a side), along with a fast readout mode and the shortest allowed number of groups (N_{groups} = 5) to minimize the saturation of the bright nuclear emission expected in the galaxy. A relatively large number of integrations (N_{ints} = 50) and four dithered exposures yielded a final exposure time of 358 s in each filter.

The raw data were downloaded from the Mikulski Archive for Space Telescopes (MAST), and processed using the *JWST* pipeline python package version 10.2 with CRDS reference files `jwst_1097.pmap`. The following sections outline the new modifications we made to the default MIRI imaging pipeline flow to improve the final imaging quality, particularly in the treatment of saturation and for corrections to the absolute astrometry.

2.1 Saturation

Even though our detector readout mode was designed to minimize saturation, some of the ramps for the nuclear pixels were still saturated due to the exceptional brightness of this AGN in the MIR. Of the ESO48-G14 images, the *F*1500*W* exposures showed 12 inner pixels around the nucleus that were flagged as saturated using the standard pipeline. Within *JWST's* up-the-ramp fitting, saturation is evident when fewer than two viable groups are accessible for a ramp fit. By default, the MIRI imager pipeline excludes the first group to bypass potential transients from the readout step between integrations (see more details in Appendix A). We display in Fig. A1, the X- and Y-profiles of the *F*1500*W* image of ESO 428-G14, spanning 6 arcsec across the nucleus. Here, we compare the default pipeline with our modified approach. We show that by turning off the first frame correction for the saturated pixels, we gained an additional

viable group, facilitating a more accurate ramp fit and subsequent flux estimation.

2.2 Astrometry

In the final stages of the pipeline reduction, absolute astrometry is established through the `tweak_registration` step. This process employs `DAOStarFinder`, a PYTHON algorithm that relies on finding background stars and/or galaxies for image alignment. Given that the galaxy fills all of the field of view (FOV) in our images, this method proves ineffective. We thus followed another approach, where we corrected the astrometry by aligning the target centroid of our images with the AGN's nuclear coordinates derived from ALMA, leveraging its high-resolution and precision as a reliable astrometric reference. By setting the nuclear position to be the peak in the ALMA 1.3 mm continuum (which emerges from very close to the SMBH), we derive a nuclear position of RA = 07^h 16^m 31.26s and Dec. = −29° 19′ 28.85 arcsec (ICRS).

2.3 Point spread function

From the three-colour *JWST* image in Fig. 1 (left-hand panel), it is evident that the point spread function (PSF) exhibits several notable effects. This includes a distinct cruciform pattern, and diffraction spikes that are due to the hexagonal shape of the mirror segments. Consequently, in order to uncover the underlying central (∼ 4 arcsec × 4 arcsec) MIR structure, image enhancement techniques such as point source subtraction and/or deconvolution become essential (see Leist et al. 2024 for a recent comparison of existing deconvolution algorithms).

We used the `WEBBPSF` package (Perrin et al. 2014) from STScI to generate PSF models at the detector position of the AGN for each of
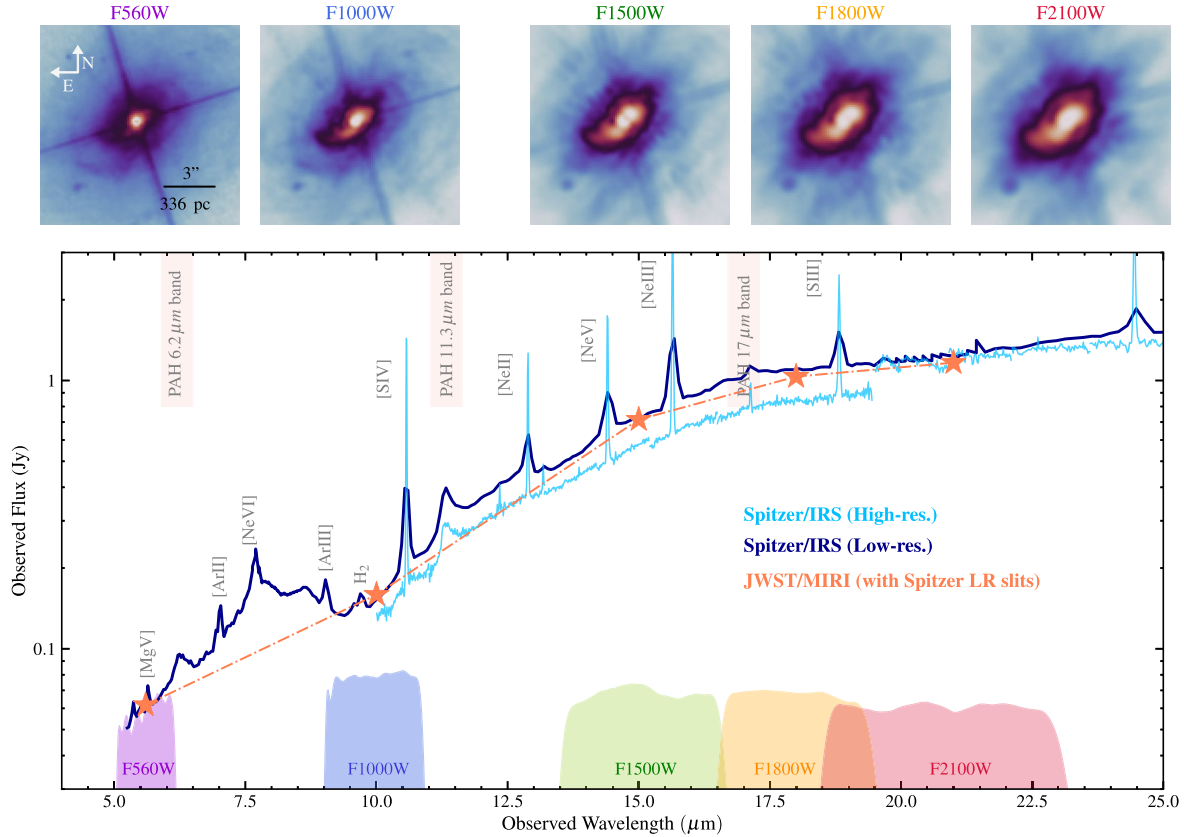
Figure 2. Top: PSF-subtracted *JWST*/MIRI images of ESO 428-G14 from the five filter bands. Each image spans a field of view of 11 arcsec×11 arcsec, with North pointing up and East to the left. Bottom: A comparison between *JWST* photometric measurements and existing *Spitzer* spectrophotometry. As a reference, key spectral features and PAH bands are identified. The depicted orange stars show *JWST*/MIRI aperture photometry, computed to mimic Spitzer's lower angular resolution at the respective wavelengths. This is achieved by convolving the images with Spitzer's PSF and computing the expected flux within the spectral slits of the Spitzer/IRS low-resolution spectrograph. The fluxes obtained are in good agreement with those from the Spitzer/IRS spectrum, an independent check on the accuracy of *JWST*/MIRI photometric calibration. The light blue curve shows the high-resolution Spitzer spectra, which show the main spectral features that lie within the *JWST* filter bandpasses (plotted along the bottom of the panel). Discrepancies in flux normalization between the two Spitzer data sets are due to the different aperture extraction methods: optimal for high-resolution, and full for low-resolution.

the four dithered images, and in each band. WEBBPSF allows the use of optimized PSFs including time-dependent wavefront distortion models and appropriate source spectral energy distributions (SEDs), both which we employ for this work. The individual PSF frames were drizzled into a single PSF model image for each band using the same image reconstruction parameters as the corresponding science images. This replicates the detector sampling effects present in the observations which can influence the final PSFs. The point source accounts for 75 per cent of the *F560W* flux at the nucleus, 57–61 per cent of the flux in the *F1000W*, *F1500W*, and *F1800W* filters, and 35 per cent of the flux in the *F2100W* filter. We show the PSF subtracted images in the top panel of Fig. 2. A more focused study on PSF modelling will be presented in Rosario et al. (in preparation).

2.4 Flux calibration

The lower panel of Fig. 2 presents a flux calibration check between *JWST* and calibrated spectroscopy from the Spitzer Space Telescope InfraRed Spectrograph (IRS; more details in Section 3.4). For each filter, we convolved the *JWST* images with the Spitzer PSF[1]

[1]The Spitzer PSF information can be found in the IRS instrument handbook.

to simulate Spitzer's optical blurring effects. Subsequent aperture photometry was then performed to calculate the total *JWST* flux within the Spitzer-defined apertures, at each wavelength. This is shown in Fig. 2 as orange stars, and is in good agreement with the SED of the Spitzer/IRS from both low-resolution (navy) and high-resolution (turquoise) spectra. The difference in normalization between the two Spitzer/IRS spectra is a result of the different aperture extraction methods used. low-resolution data is presented using the full aperture extraction method, while high-resolution data is displayed using the optimal extraction method, which ensures a high signal-to-noise ratio and employs a smaller aperture size (see Lebouteiller et al. 2011).

3 ARCHIVAL DATA

We compiled data from several observations, which we describe in more detail below. The ALMA, HST, and VLA data were employed to understand the structure and origin of the extended MIR emission within the broader context of this galaxy (see Section 4.3). Meanwhile, the VLT/SINFONI and the Spitzer/IRS data were used to compute and correct for emission line contamination (see Section 4.4).

3.1 VLT/SINFONI spectroscopy

K-band (1.9–2.5 μm) IFU data were obtained with the Spectrograph for INtegral Field Observations in the Near Infrared (SINFONI) on the European Southern Observatory (ESO) Very Large Telescope (VLT; Eisenhauer et al. 2003; Bonnet et al. 2004). The data were collected on 2010 December 22 and 2011 January 11, under Program 086.B-0484 (PI: Mueller Sanchez). Observed in natural guide star mode, the data cover a roughly 4 arcsec × 4 arcsec field of view with a spectral resolution of $R \approx 1500$. A standard Object-Sky-Object observation sequence was used with each integration lasting 300 s for a total on-source time of 60 min. Data reduction was carried out with the SINFONI Data Reduction Software. This data reduction pipeline included all standard routines needed for the near-infrared (NIR) spectra as well as additional routines used for construction of the data cube. Enhanced subtraction of the OH sky line emission was implemented as outlined by Davies (2007), and telluric correction and flux calibration was carried out using B-type stars. The calibration uncertainty is about 10 per cent in flux as determined from the standard deviation of aperture photometries of the individual dithered cubes before combining to create a final data cube.

The emission line flux maps were generated using the custom IDL code LINEFIT (Davies et al. 2011), which fits the emission line of interest with an unresolved line profile (a sky line) convolved with a Gaussian, as well as a linear function to the line-free continuum. This single-component Gaussian fitting procedure was performed for each spaxel of the data cube. Flux and kinematic information were extracted from the Gaussian fit and, in conjunction with the spatial information of each spaxel, used to generate the line maps for [Si VI]λ1.96 μm, Brγ [2.16 μm] and H_2 1–0 S(1) [2.12 μm] emission lines. A more detailed analysis of the [Si VI] and Br γ lines is presented in May et al. (2018).

3.2 ALMA spectroscopy

We extracted ALMA Band 6 data products for ESO 428-G14 from the ALMA Science Archive in rest frequencies of 230.538 and 232.538 GHz corresponding to the CO (2-1) line and the 1.33 mm continuum emission, respectively. ESO 428-G14 was observed by ALMA on the 12th of May, 2016 (progam ID: 2015.1.00086.S, PI: Neil Nagar). The FOV is 24″.52 across, effectively covering the entire circumnuclear region. We processed the data using the CARTA software package and generated a flux map with a 2σ cut. A more detailed analysis of these data was conducted by Feruglio et al. (2020).

3.3 *HST* images

We retrieved fully reduced *HST*/WFPC2 images of ESO 428-G14 from the Hubble Legacy Archive (progam ID: 5411, PI: Andrew Wilson). The observations were carried out on 17 April 1995, with exposures with the narrow-band *F*658*N* filter lasting a total of 13.33 min and exposures with the broad-band *F*814*W* filter lasting 3.33 min. We follow Falcke et al. (1998) and refer to the *F*658*N* image as the Hα image, despite the 33 per cent contribution from the [N II]λλ6548, 6584 lines. A detailed analysis of this data was carried out by Falcke et al. (1996, 1998).

To correct the astrometry of the HST images, we aligned it with the positions of stars identified from the GAIA DR3 catalogue (Gaia Collaboration 2016, 2023). These accurately identified stars within the HST images serve as precise astrometric reference points.

3.4 *Spitzer* IRS spectra

We retrieved fully reduced low- and high-resolution MIR spectra (program ID: 30572, PI: Varoujan Gorjian) from the Combined Atlas of Sources with Spitzer/IRS Spectra (CASSIS; Lebouteiller et al. 2011). The spectra, taken in IRS staring mode, were extracted using the optimal extraction method for high-resolution data to achieve the best signal-to-noise ratio, which is equivalent to a point source extraction. On the other hand, the low-resolution data were obtained using the full-aperture extraction method.

3.5 VLA

We extracted high-frequency (15 GHz, 2 cm) Very Large Array (VLA) *U*-band radio data from National Radio Astronomy Observatory data archive (PI: Heino Falcke). The radio core coordinates (RA, Dec.) can be found in table 3 of Falcke et al. (1998) and are RA = 07^h 16^m 31.207^s and Dec. = $-29°$ 19′ 28.89 arcsec (ICRS). The data reduction was performed as described in section 2.2 of Falcke et al. (1998). Astrometry corrections were done by placing the radio peak at the [Si VI] flux peak.

4 RESULTS

4.1 Characteristics of the MIR morphology

The new *JWST*/MIRI images (Fig. 1) provide a comprehensive view of the galaxy's various MIR characteristics, revealing new details in its centre. The image is dominated by a pronounced cross-shaped pattern of diffraction spikes, a manifestation of the very bright nuclear point-like MIR source spread out through *JWST*'s intricate PSF. Both the *JWST* and HST images share a number of key features, including a circumnuclear dusty disc that appears as annular rings, which corresponds to faint, tightly wound spiral arms.

These arms extend all the way to the nucleus, which appears prominently bright in both images in Fig. 1. ESO 428-G14 harbours in its heart a well-collimated radio jet (inset in righthand panel of Fig. 1) that is partially shaped by its interaction with the disc (Falcke et al. 1996, 1998).

The five single-band PSF-subtracted MIR mosaics revealing the resolved centre of ESO 428-G14 are presented across the top of Fig. 2. Residuals from diffraction spikes, particularly in the *F*560*W* filter, remain even after subtraction of the nuclear PSF, indicative of the high surface brightness central emission in the images. While the *F*560*W* image provides the best overall resolution, it does not reveal the nuclear extended structure prominently. This structure only emerges in the *F*1000*W* filter and in the longer-wavelength bands. However, in the images in these latter bands, the resolution gets steadily worse as the PSF broadens. We thus use the *F*1000*W* image as a baseline to study the nuclear extended structure, as it provides a good compromise between resolution and the visibility of the extended MIR features. For the remainder of the paper, we refer to the extended MIR structure seen in the central 4 arcsec × 4 arcsec, after subtraction of the nuclear point source, as the 'extended MIR emission'.

We find that the extended MIR emission exhibits a notable asymmetry, with distinct North-Western and South-Eastern regions extending along a similar PA to the radio jet of ∼ 131 deg, measured North to East. To the North-West, the emission adopts a compact structure and extends up to ∼ 150 pc from the nucleus. The South-Eastern emission is more extended, revealing two strands that diverge from the main structure, pointing northward. These can extend up
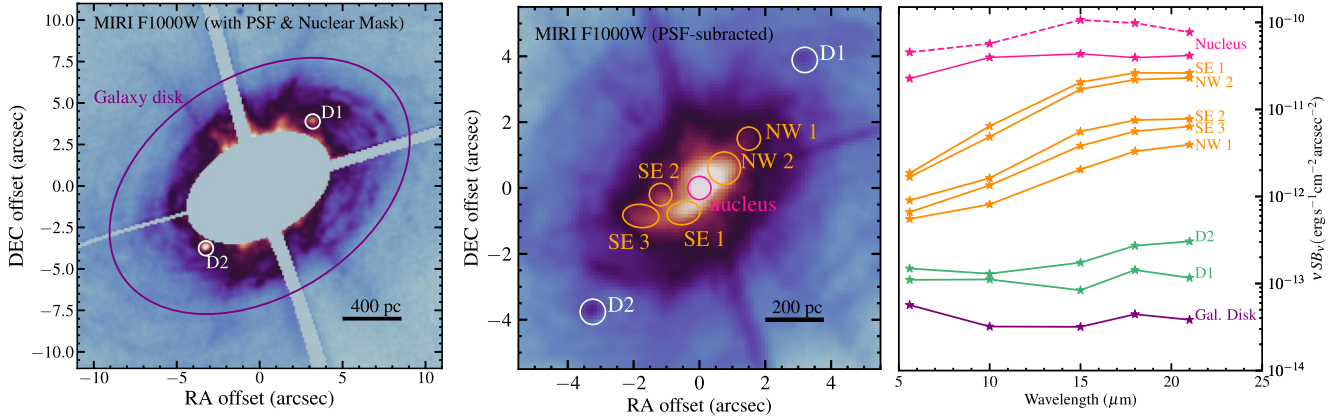
Figure 3. Left: The *JWST*/MIRI *F*1000*W* PSF-subtracted image showing the full galaxy disc and the aperture used to perform photometry on the disc emission (purple ellipse). The extended nuclear emission as well as the strongest diffraction spikes from the nucleus are masked out to enable a cleaner assessment of disc emission. Two bright regions on the disc are noted as D1 in the North West, and D2 in the South East (white circles). Middle: A zoom into the inner ~ 10 arcsec $\times$ 10 arcsec region of the PSF-subtracted *F*1000*W* image to reveal the extended MIR morphology. Regions of interest along the central 400 pc structure are marked in orange (NW1, NW2, SE1, SE2, SE3), while regions that appear within the disc are marked in white (D1, D2). Right: Spectral energy distributions (SEDs) of the reduced surface brightness (SB), computed using PSF subtracted images across the *JWST*/MIRI bands for all regions, including the nucleus and the disc. For the nucleus, the dashed line is derived from the original images, while the solid line is produced using PSF-subtracted images. Note that the SB of the disc includes D1 and D2. Error bars are included in the plot but are too small to be visible.

Table 1. The selected regions of interest as outlined in Fig. 3.

Region[1]	Δ RA[2]	Δ Dec.[3]	Aperture[4]	F_{F560W}	F_{F1000W}	F_{F1500W}	F_{F1800W}	F_{F2100W}	%([S IV]/F1000W)[5]
Nuclear[a]	0	0	0."35	85.31	189.40	536.15	588.54	534.53	
Nuclear[b]	0	0	0."35	16.00	51.00	84.00	91.00	112.00	6
NW1	1.46	1.38	0."35	0.41	1.04	3.99	7.70	10.62	
NW2	0.97	0.47		2.42	12.39	65.92	101.31	122.91	30
SE1	−0.56	−0.72	(0."50, 0."35, −80°)	1.95	11.95	57.72	88.27	101.72	15
SE2	−1.51	−0.38	0."35	0.65	2.10	10.89	17.56	21.06	35
SE3	−2.08	−1.00	(0."55, 0."35, −95°)	0.75	2.71	11.65	20.42	26.85	40
D1	3.44	3.89	0."4	0.096	0.17	0.19	0.39	0.37	
D2	−3.85	−3.76	0."4	0.13	0.20	0.40	0.75	0.98	

Note. (1) Regions of interest (refer to Fig. 3). For the nucleus, we present two SEDs, one derived from (a) the original images (dashed pink line in Fig. 3), and the other from (b) the PSF-subtracted images (solid pink line, Fig. 3). For all the other regions, the SEDs are derived using PSF subtracted images. (2 and 3) The relative positions are given as offsets from the nucleus (RA$_{nuc}$ = 07^h 16^m 31.26^s and Dec.$_{nuc}$ = −29° 19' 28.85 arcsec) in arcseconds. (4) The aperture radius is provided in arcseconds, showing a single value for circular apertures and three parameters (semimajor axis, semiminor axis, PA measured N-E) for elliptical apertures. (5) When possible, we provide the average percentage of line emission contribution to the total flux (in the case of the *F*1000*W* filter. All fluxes across various filters are measured in units of 10^{-3} Jy.

to ~ 300 pc from the nucleus. The total extent of the extended MIR emission is ~ 450 pc. As we will show in Section 4.3, the overall structure resembles that of the H α line and the radio jet from Falcke et al. (1996, 1998).

4.2 MIR regions of interest

We leverage the optimal resolution and sensitivity of the *F*1000*W* image to define regions of interest within the nuclear and extended MIR structure, as depicted in the middle panel of Fig. 3. We then examine and compare the MIR spectral energy distributions of these regions, measured in fixed sized apertures, to explore their properties. The regions and details of the apertures are given in Table 1.

The nuclear aperture is centred on the nuclear position. NW1 and NW2 are situated in the North-West region, while SE1, SE2, and SE3 map out the two strands that split from the main structure towards the South-East.

We also identified two interesting regions, D1 (07^{h}16^{m}30.97^s, −29°19'24.90 arcsec) and D2 (07^{h}16^{m}31.46^s,

−29°19'32.55 arcsec), that lie beyond the extended MIR emission, but along a similar PA to it and to the radio jet. Unlike most of the galaxy disc, these regions appear prominently red in the map of the colour *F*560*W*–*F*1000*W* (see Fig. B1 in the Appendix). Their location and relationship to the extended MIR emission suggests that the AGN could play some part in their heating. Indeed, recent work by Hermosa Muñoz (2024, submitted) detect multiple MIR knots along the direction of the outflow in another nearby Seyfert galaxy, NGC 7172. The left-hand panel of Fig. 3 zooms out to show the full circumnuclear disc. We define an aperture mask that excludes any contribution from the nuclear or extended MIR emission, as well contamination from diffraction spikes from the nuclear point source. This aperture gives an averaged SED for the circumnuclear disc free of much emission influenced strongly by the AGN.

For all identified regions, we select apertures with diameters bigger than the PSF FWHM of the longest wavelength filter (i.e. *F*2100*W*, FWHM = 0."67). This minimizes the need to include detailed aperture corrections in the SEDs with increasing wavelength (see Table 1). The right-hand panel of Fig. 3 shows the five band SEDs,
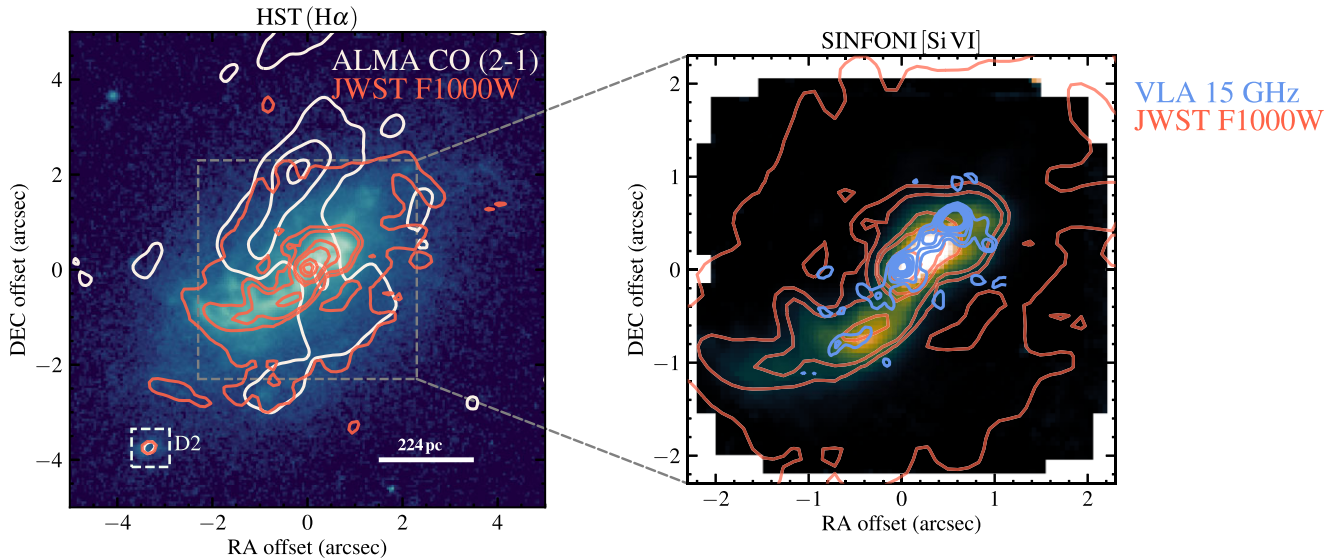
Figure 4. Left: The HST Hα image of ESO 428-G14, with the nucleus at the centre. Superimposed red contours depict the *JWST* PSF-subtracted *F*1000*W* image, while the white contours are for the ALMA CO (2-1) moment 0 map. The position of the SE region D2 (see Fig. 3 as a reference) is highlighted by the white square. Right: Zooming into the inner ∼ 4 arcsec × 4 arcsec to match the FOV of SINFONI, we display the [Si VI] flux map. The red contours are from the *JWST* PSF-subtracted *F*1000*W* image (comparable to the left-hand panel), while light blue contours map the VLA radio 2 cm (15 GHz) image.

expressed in units of reduced surface brightness ($\nu \, SB_\nu$), of these different regions. Across all filters, regions closer to the nucleus and within the direct influence of the AGN, are characterized by high SB. The regions farther out, identified with the galaxy disc, exhibit lower SB.

The highest SBs are found in the nuclear aperture (pink line), particularly at shorter wavelengths ($\lambda_{cent} \leq 10 \, \mu m$). For completeness, we also add in Fig. 3 and Table 1 the nuclear SED derived from the original images (dashed pink line), which includes the PSF. This shows a peak around ∼ 15 μm. The nuclear SED derived using the PSF subtracted images (solid pink line) is flat, with a SB_{F560W}/SB_{F2100W} ratio of ∼ 0.56, and remains consistently bright across all filters. This indicates that the nuclear region emits a substantial portion of energy (∼ 20 per cent of the total *F*1000*W* flux), which does not significantly change at longer wavelengths. This flat SED can be attributed to dust with a blend of temperatures from various components in the vicinity of the AGN, out to ∼ 40 pc, reflecting a complex thermal environment rather one with a single uniform temperature.

Moving towards regions in the extended emission structure, we find that all regions identified within it (in orange) are characterized by steeper SEDs, defined by their SB_{F560W}/SB_{F2100W} ratios of ∼ [0.07 − 0.1]. Lower values of this ratio indicate substantial increase in flux at longer wavelength, while values closer to unity would imply a flat SED. Assuming a simple blackbody, we estimate temperatures within the range ∼ 100 − 120 K for the regions in the extended emission. The highest temperatures are found in SE1 and NW2, likely due to their close proximity to the nucleus. These values serve as an approximation (based on five photometric points), and a more advanced fitting method is required to accurately estimate the temperature.

In contrast to the extended emission regions influenced by the AGN, the average galaxy disc has a relatively flat SED. The rise we observe towards the shortest wavelengths could come from low levels of stellar light in the MIR, the tail of the combined photospheric emission from stars in the disc. A slight excess in the *F*1800*W* band

over a flat SED shape could arise from the contribution of Polycyclic Aromatic Hydrocarbon (PAH) bands at 17 microns (indicated in Fig. 2; see García-Bernete et al. (2022) for a detailed discussion). We interpret the flatness of the star-forming galaxy disc in a similar way as we do for the AGN nucleus: the disc consists of amalgamated dusty star-forming regions with a range of temperatures set by distributed heating. Because stars are not as powerful heating sources as the AGN, the SB of the disc is low.

Turning to the regions D1 and D2 that appear to be on the galaxy disc (although might also lie along the outflow direction), these display flatter SB profiles similar to the galaxy disc. Their SB ratios of $SB_{F560W}/SB_{F2100W} \approx [0.7 − 0.95]$ highlight the flatness of these SEDs. For this reason, we suggest that these features are star-forming regions. While both D1 and D2 share this characteristic, both show minor differences in SEDs, indicating variation in the star-formation heating. The elevated surface brightness in the *F*1800*W* band is especially apparent in region D1, which again suggests a possible PAH contribution. Estimating a temperature for these SF regions would require accounting for PAH, which is beyond the scope of this paper.

4.3 A multiwavelength view

The most remarkable find from Fig. 4 is the striking morphological resemblance between the MIR emission, the HST Hα image and the [Si VI] emission. This agreement may suggest that the processes influencing the ionized gas and the MIR emission (arising from dust) in the nuclear region may be the same, or that the MIR emission is not solely attributable to dust (see next Section 4.4).

In the left-hand panel of Fig. 4, the CO (2-1) structure appears to trace an inner feature near the vicinity of the SMBH. Feruglio et al. (2020) describe this as a transverse gas lane that is bridging two segments of a circumnuclear ring, and feeding the SMBH by channeling material to it. Our observations reveal both the MIR structure and Hα emission to be perpendicular to this 'feeding' lane, implying a polar configuration. This is also supported by

the alignment of the radio jet with the extended MIR structure, as discussed in Section 4.1. This multiwavelength view uncovers that D2 is also detected in H α and CO (2-1) emissions (see left-hand panel, Fig. 4), strengthening the case for its SF nature.

The radio morphology, with an extent of ~ 2 arcsec along PA$\approx 131°$, reveals more intricate details, especially towards its hotspot in the North-West. Here, it captures two clumps that are not resolved in the *JWST*/MIRI images (see NW2 in Fig. 3). This feature has been previously identified in HST Hα imaging by Falcke et al. (1996) and in the SINFONI Brγ map by May et al. (2018).

4.4 Emission line contamination

JWST/MIRI images are obtained using broad-band filters that span a few microns around the central wavelength. This means that the filters can capture both the continuum emission from dust and any line emission from gas that falls within the filter's wavelength range. As can be seen in the bottom of Fig. 2, the five imaging filters used in this study overlap with a couple of emission lines and PAH bands that could contribute to the MIR emission, potentially influencing the morphology seen. This includes the $F1000W$ filter, which can be contaminated by the [S IV] and H$_2$ 0–0 S(3) lines; $F1500W$, by [Ne V] and [Ne III] lines; and $F1800W$, where PAH bands and the [S III] line may impact the observed emission. Moreover, the mutliwavelength analysis in Fig. 4 shows a striking correlation between the MIR structure, [Si VI], and H α emissions, which could be explained (in part) by strong emission line contribution in the *JWST* images. This could influence our interpretation of the observed MIR structures, attributing features to dust continuum that may, in fact, be closely connected to ionized or molecular gas instead.

The absence of any high-resolution *JWST* spectroscopy for ESO 428-G14, such as from the MIRI Mid-Infrared Spectrograph (MIRI/MRS), complicates this analysis, as it would otherwise provide a clearer distinction between dust and gas contributions to the observed MIR structure. To overcome this limitation, we leverage the wealth of multiwavelength information for this galaxy to develop a method to estimate the level of emission line contamination in the $F1000W$ image. As discussed before, this filter provides the highest resolution of the inner (4 arcsec × 4 arcsec) extended MIR structure, and is thus the ideal band for our assessment of contamination along that region.

From Fig. 2, one can see that both the [S IV] line at $10.51\,\mu$m and the H$_2$ line at $9.65\,\mu$m fall within the $F1000W$ filter bandwidth, which means they can contaminate this image. To check this, we produced mock maps for H$_2$ and [S IV]. Our methodology can be applied to any filter and is described as follows. First, we leverage the Spitzer/IRS SH spectrum (when possible, otherwise low spectral resolution) to estimate the total flux due to each line. Second, we use these estimates to scale a SINFONI line map of comparable ionization potential (IP) to ensure similarity in morphological characteristics. This then produces a mock map for the line in question, providing us with a proxy for its expected spatial distribution.

It is important to note that the ionization potential can significantly influence the morphology of the emission line. A recent *JWST* study by Pereira-Santaella et al. (2022) demonstrate that MIR lines with higher IPs tend to be more compact compared to those with lower IPs. Another caveat that should be kept in mind is extinction, which is very low for this object and thus has no impact on the measurements made. Nevertheless, this method allows us to estimate the extent of emission line contribution within the *JWST* $F1000W$ image, thereby revealing regions with significant contamination. Our method has been validated against another nearby Seyfert from the GATOS

survey, NGC 5728, for which we have both imaging and spectroscopy (see upcoming sample paper Rosario et al. in preparation). We describe in more detail below the steps taken to produce each mock map.

4.4.1 [S IV] mock map

Using Spitzer/IRS SH spectrum (see Fig. 2), we fit the [S IV] emission line with a single-component Gaussian, yielding a total flux of $f_{SIV} = 7.564 \times 10^{-13}$ erg/s/cm^2. To generate a mock [S IV] map, we used the Br γ map as morphology template. Riffel et al. (2006) demonstrated that Br γ is in good correspondence with the radio jet, with some signatures of shocks. As such, we assume that there is little to no SF contribution in this line. We also note that Br γ has an IP of 13.6 eV that can be comparable to that of [S IV] (35 eV), so the extent of their emissions will not differ by much. The mock map is then produced by scaling the Brγ map to match the expected flux from [S IV], f_{SIV}.

The level of [S IV] contamination is quantitatively assessed by calculating the ratio between the mock [S IV] map (panel a in Fig. 5) and the PSF-subtracted *JWST* $F1000W$ image (panel b in Fig. 5). The ratio map, as seen in Fig. 5 (panel d), unveils how the [S IV] contamination level varies spatially across the extended MIR morphology. Overall, the median contribution of [S IV] across the entire extended MIR structure is approximately 15 per cent. Notably, structures extending ~ 1 arcsec from nucleus, both towards the NW and SE regions, are the most impacted, with contamination levels reaching up to 45 per cent.

4.4.2 H$_2$ mock map

We extracted from Spoon et al. (2022) the total flux arising from the H$_2$ 0–0 S(3) [$9.65\,\mu$m] line as $F_{tot, H_2} = (9.2 \pm 1.6) \times 10^{-21}$ W cm^{-2}, computed using Spitzer/IRS low-resolution spectral data. With this value, we scaled the SINFONI H$_2$ 1–0 S(1) [$2.12\,\mu$m] map to produce a mock map for H$_2$ 0–0 S(3) [$9.65\,\mu$m] line (panel c in Fig. 5). We then computed a contamination map as a ratio between the mock H$_2$ 0–0 S(3) [$9.65\,\mu$m] map and the $F1000W$ image (panel e in Fig. 5). This gives a very weak contribution of H$_2$ 0–0 S(3) [$9.65\,\mu$m] line to the extended MIR emission, varying between 2 and 4 per cent.

4.4.3 Pure dust continuum morphology

To reveal the true morphology of the dust, we subtracted the total flux contribution arising from both the [S IV] and H$_2$ from the $F1000W$ PSF subtracted image. From the maps computed in Fig. 5, it is clear that H$_2$ contributes negligibly to the total MIR emission, with a contamination level of 4 per cent at its highest. In contrast, the [S IV] line accounts for nearly half of the extended emission, establishing it as the primary contaminator. Consequently, we boosted the [S IV] flux by 4 per cent to account for the H$_2$ contribution. Following this, we subtracted the boosted [S IV] map from the PSF-subtracted $F1000W$ image and produced a contamination free image, as shown in right-hand panel of Fig. 6. This image brings to light the structure of the 'pure continuum'. Indeed, the brightness of the MIR structure significantly drops in the SE and NW. This affects the appearance of the South-Eastern strands which are now too faint to notice. As a result, the structure of the dust appears more compact and concentrated around the nucleus. When compared to the regions of interest presented in Fig. 3 and Table 1, it becomes evident
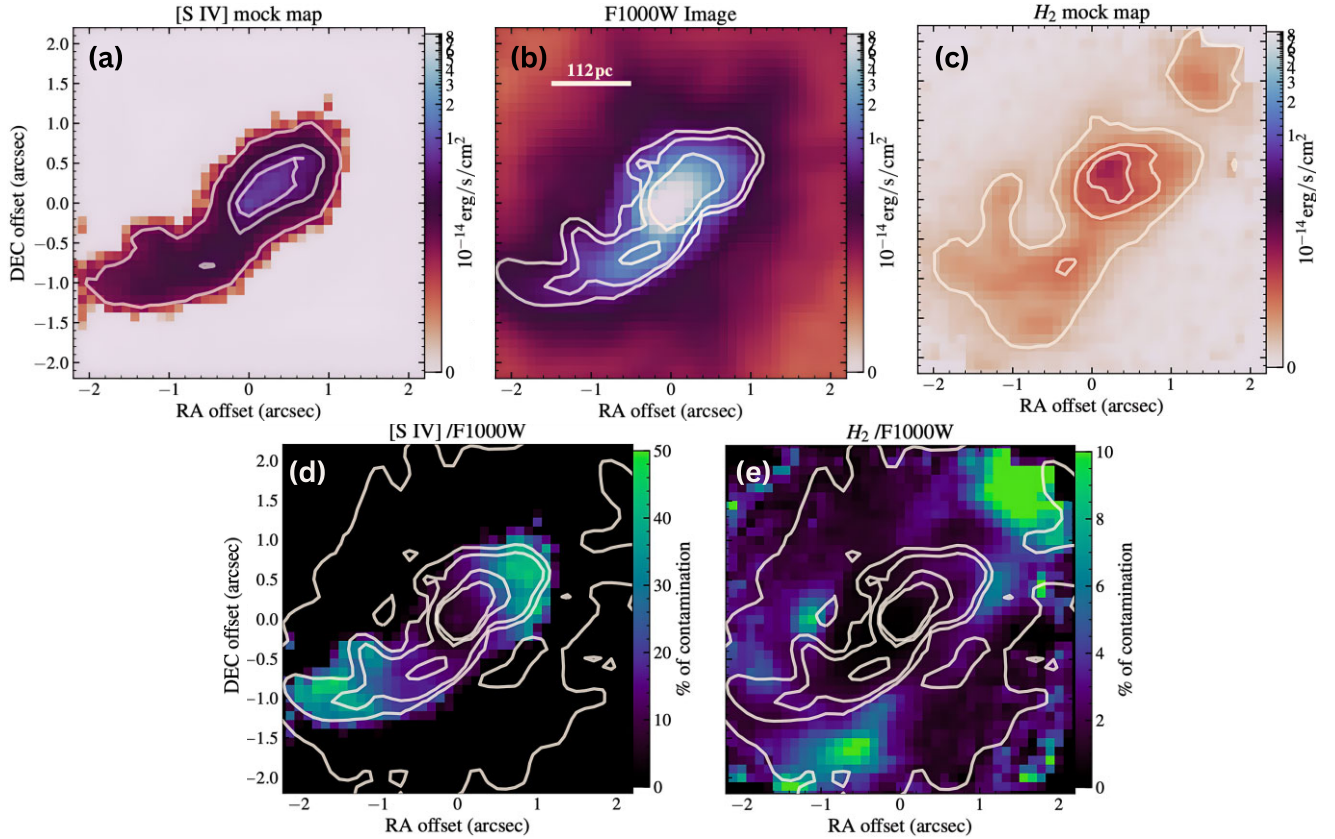
Figure 5. Emission line mock maps and the associated contamination maps with respect to the $F1000W$ image. The top three panels share the same logarithmic scale and stretch, allowing for a direct visual comparison of the relative flux. For each panel, contour levels represent $(2,10,50)\,\sigma$ levels. (a) Mock [S IV]$\lambda 10.51\,\mu$m map computed using Brγ from SINFONI as a template. (b) The PSF-subtracted $F1000W$ *JWST*/MIRI image. (c) Mock H_2 0–0 S(2) [9.65 μm] map using H_2 1–0 S(1) [2.12 μm] from SINFONI as a template. (d) Spatial distribution of contamination percentages of [S IV] within the $F1000W$ image. Overlaid contours are from the *JWST* image to show the extent of the MIR morphology. (e) Same as before but for H_2 contamination level.

that contamination levels rise with increasing distance from the nucleus. For example, the South-Eastern regions, SE2 and SE3, exhibit contamination levels ($\sim$35 per cent and 40 per cent) at least twice as high as that of SE1 ($\sim$ 15 per cent), resulting in their diminished appearance in Fig. 6.

Compared to the original polar and extended MIR structure presented in lefthand panel of Fig. 6, the new 'dust only' image shows that it reduced by more than half of its original size. The new total extent of the dust is roughly $\sim$ 1.8 arcsec ($\sim$ 200 pc) in size, stretching $\sim$ 0.8 arcsec to the NW and $\sim$ 1 arcsec to the SE from the nucleus. However, it still exceeds the traditional limits of the torus ($\sim$ tens of parsecs). Moreover, we find a striking correspondence between the extent and morphology of the polar dust and the radio jet (see right-hand panel, Fig. 6). We explore in Section 5 all possible origins of this polar dust.

5 DISCUSSION

5.1 Dust beyond the torus

The exceptional resolution and sensitivity of *JWST*/MIRI allowed, for the very first time, the imaging of the MIR heart of ESO 428-G14, revealing new details about its structure and properties. In the central $r \approx 2$ arcsec region of ESO 428-G14, we detect a bi-polar structure extending up to $\sim$ 450 pc in size, from the NW to the SE. In contrast to the galaxy disc, our SED analysis reveals that regions

along the polar MIR structure emit strongly in the MIR, and are characterized by warm temperatures ($T_{dust} \approx 120$ K) and steep SEDs (SB$_{F560W}$/SB$_{F2100W} \approx 0.07$), especially for regions (NW2, SE1) that are adjacent to the nucleus. Such trends in the MIR strongly suggest the presence of warm dust along these regions.

Our multiwavelength analysis (Fig. 4) points towards a strong correlation between the structure of the extended polar MIR emission and that of multiple emission lines from ionized gas ([Si VI], Hα, Br γ). We attribute this, in part, to a significant contribution of emission lines in *JWST*/MIRI broad-band imaging that contaminate the MIR morphology (Section 4.4 and Fig. 5). While it is challenging to disentangle gas and pure dust structures in the absence of MIR spectroscopy (e.g. from the *JWST*/MIRI MRS), an important aspect of this study is the development of a method to estimate the level of line contamination using existing pre-*JWST* data sets (see Section 4.4 for more details). Using the image in the $F1000W$ filter, an optimal band for the contrast of extended MIR emission, we produced a pure continuum version that reveals that the dust is indeed more compact, with a total length of $\sim$ 200 pc (Fig. 6) – shrinking to half of its original length ($\sim$ 450 pc).

The question now arises regarding the nature of this polar dust. Prieto et al. (2014) computed an extinction map for ESO 428-G14 (see their Fig. 8), revealing dust structures with weak spirals which are reminiscent of the morphology seen in CO (2-1) emission from ALMA (Feruglio et al. 2020, their Fig. 1). These structures are indeed different from the polar structure seen in Fig. 6. As such, the dust
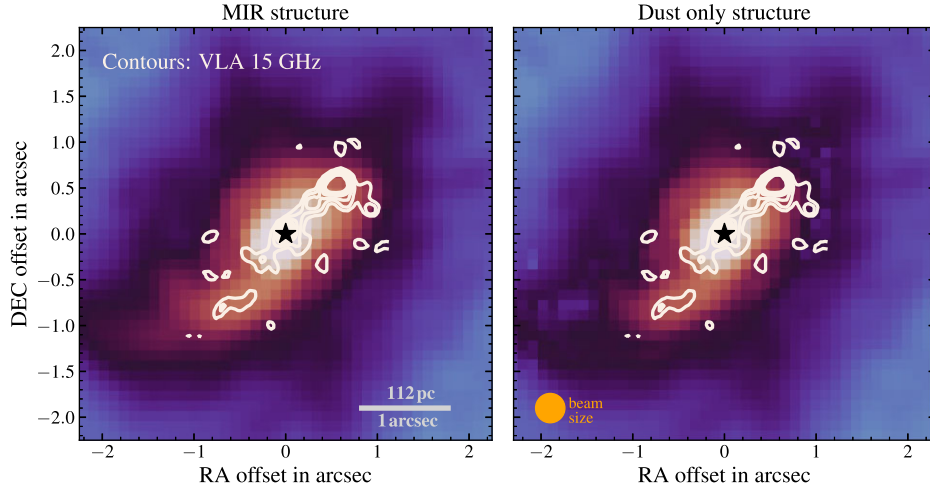
Figure 6. Left: The original polar and extended MIR structure from the PSF-subtracted *F1000W* image. Contours show the VLA 15 GHz emission which traces the radio jet. The black star marks the position of the nucleus. Right: The pure continuum or 'dust-only' image obtained after subtracting the emission line contributions from the PSF-subtracted *F1000W* image. The dusty structure shows good spatial correspondence to the radio jet, including an asymmetry in the NW extent compared to the SE extent. The orange circle in the bottom left shows the FWHM (0″.32) of the *F1000W* PSF. Both images are displayed on a logarithmic scale and share the same stretch to highlight the differences before and after decontamination.

probed with *JWST* is not normal cold dust in the galaxy, but it could be dust in the NLR illuminated by AGN radiation fields, local dust heated by jet-induced shocks, or dust driven by a wind from the torus. We discuss each of these possible scenarios in more detail.

5.2 Dust illuminated in the NLR

The simplest explanation of the polar dust would be the illumination of ambient dust within the NLR by the AGN's radiation. Such a scenario accounts for the observed spatial correlation with ionized emission line regions because both phases are produced by the same radiation field. This explanation does not require any connection between the dust and outflows from the AGN. Here, we test whether heating/illumination from the central engine alone is able to explain the observed temperatures along the polar MIR emission.

As an exercise, we take the region NW2 (Fig. 3) as a case study, at a distance $D \approx 100$ pc from the nucleus. To compute a bolometric luminosity for the AGN, we applied a bolometric correction according to equation (3) in Duras et al. (2020) to the hard X-ray luminosity of $L_{2-10\,\mathrm{keV}} = 3.6 \times 10^{41}$ erg s^{-1} reported by Levenson et al. (2006). This gives $L_{\mathrm{bol,\,AGN}} = 5.5 \times 10^{42}$ erg s^{-1}. This value is comparable to the estimate of the AGN's bolometric luminosity from its integrated MIR luminosity of $2 \pm 1 \times 10^{42}$ erg s^{-1} from (May et al. 2018).

We express the expected anisotropic radiation field in terms of the Habing field, following Tielens (2010) (chapter 5, equation 5.43):

$$G_0 = 2.1 \times 10^4 \left(\frac{L_{\mathrm{bol,AGN}}}{10^4 L_\odot} \right) \left(\frac{0.1\,\mathrm{pc}}{D} \right)^2. \tag{1}$$

Then, for dust grains with a size a, the equilibrium dust temperature can be expressed as:

$$T_d \approx 33.5 \left(\frac{1\,\mu m}{a} \right)^{0.2} \left(\frac{G_0}{10^4} \right)^{0.2} \mathrm{K}, \tag{2}$$

following Tielens (2010) (chapter 5, equation 5.44). An important assumption here is that the intrinsic AGN SED that heats the dust peaks strongly in the UV, roughly like the local Habing field.

Assuming classical ISM dust grains within the range of $a = 0.005 - 0.25\,\mu\mathrm{m}$ (Draine & Lee 1984, see their discussion around

equation 5.1), the expected dust temperature at distance $D \approx 100$ pc from central source with the assumed $L_{\mathrm{bol,\,AGN}}$ would be $T_{\mathrm{dust}} = [76, 35]$ K, where the lower temperature corresponds to the largest grain size. Therefore, assuming the absorption-averaged grain size is at the lower end of size distribution, reasonable for ISM dust, illumination along the NLR can heat the dust only up to several tens of K. This is lower than the dust temperatures we estimate for the NW2 region.

Note that the temperature may be a bit higher than our estimates if X-ray heating of dust is efficient, because AGN have a higher proportion of X-ray energy compared to the Habing field. Additionally, in the ionized gas phase, resonance trapping of Ly α, which leads to complete reprocessing of these UV photons, can also raise the temperature of the dust associated with this phase.

5.3 Dust originating from the torus

At the inner edge of the torus, infrared radiation pressure applied on dust grains can lift the dust radially outward, leading to a polar dusty wind (e.g. Hönig et al. 2012). Semi-analytical models produced by Venanzi et al. (2020) confirm that it is possible for dusty winds to be launched from the inner regions of the torus. Their work also predicts radiation pressure to be more efficient at driving this wind around a critical limit, where AGN radiation pressure and gravity from the black hole are balanced.

Some studies have proposed that the column density – Eddington ratio ($N_H - \lambda_{\mathrm{Edd}}$) plane can be used as a diagnostic to infer the conditions under which radiation pressure dominates over gravity, thereby giving rise to radiation-driven outflows (e.g. Fabian et al. 2008; Ricci et al. 2017; Venanzi et al. 2020; Alonso-Herrero et al. 2021). For ESO 428-G14, Feruglio et al. (2020) estimated the line-of-sight H_2 column density to be $N_{H_2} \approx 2 \times 10^{23}$ cm^{-2}, but report this as a lower limit due to beam dilution. This equates to a hydrogen column density of $N_H \approx 4 \times 10^{23}$ cm^{-2}. Using the $M_{BH} - \sigma_\star$ scaling relation, Fabbiano et al. (2019) derived an estimate for the BH mass of $M_{BH} \approx (1 - 3) \times 10^7$ M$_\odot$. With this BH mass and the AGN bolometric luminosity derived earlier ($L_{\mathrm{bol,AGN}} = 5.5 \times 10^{42}$ ergs^{-1}), we compute an Eddington ratio within the range of $\log_{10} \lambda_{\mathrm{Edd}} \approx$

$(-2.83, -2.36)$, consistent with the system's previously accepted status as a relatively weak AGN. This sets ESO 428-G14 in a region of the $N_H - \lambda_{Edd}$ plane where outflows are not efficiently driven.

It is worth noting that the substantial systematic uncertainties on M_{BH}, $L_{bol,AGN}$ and N_H can shift the position of the AGN around on this diagram. The strength of the wind and its orientation depend on λ_{Edd} and n_H (e.g. Ricci et al. 2017; Venanzi et al. 2020), which are not well-constrained for the heavily obscured AGN in ESO 428-G14. We also note that, while the $N_H - \lambda_{Edd}$ plane defines the ideal region for launching radiation driven winds, such outflows are still found in AGN that lie outside the region.

Torus models that include a self-consistent wind component predict the wind originates at the sublimation edge of the torus (Hönig et al. 2013; Hönig & Kishimoto 2017). Consequently, the composition of the dust within the wind is expected to be similar to that of the sublimation region, where small dust grains, particularly silicates, are easily destroyed (e.g. Hönig & Kishimoto 2017; González-Martín et al. 2023). As such, it is primarily the larger dust grains of size ($a \approx 0.075 - 1\,\mu$m) and graphites that are robust enough to survive in the sublimation region and as a result, in the dusty wind (e.g. Hönig & Kishimoto 2017; Hönig 2019). Using equations (1) and (2), but taking the larger grain sizes expected in the wind, the temperature of the polar dust would be $T_{dust} = [44, 26]$ K at $D \approx 100$ pc from the nucleus. This is much lower than the estimated temperature of the extended polar dust in NW2. Therefore, we do not expect that the dust we see in the extended MIR emission is deficient in small grains. This adds credence to its origin as ambient ISM dust. While a polar dusty wind may still be present in ESO 428-G14, it would be too small for our images to resolve, lying well within the nuclear aperture as defined in Section 4.2.

5.4 Dust heated by shocks

Fig. 6 reveals the polar dust to be co-spatial with the radio jet, which could indicate that shocks induced by jet–ISM interactions are an important culprit in heating the dust. Indeed, previous studies have shown that the radio jet in ESO 428-G14 is coupled with the disc and shows spatial correspondence with a number of emission lines, indicating that the radio jet can strongly perturb the ionized gas (e.g. Falcke et al. 1996; Riffel et al. 2006; May et al. 2018).

Evidence of shocks in ESO 428-G14 in the central ~ 200 pc has been reported in a number of previous studies. For instance, Riffel et al. (2006) find that the radio jet can contribute up to 90 per cent to the excitation of [Fe II]1.257 μm, with strong enhancement in the [Fe II]/Paβ ratio along the jet region. Additionally, CLOUDY modelling by May et al. (2018) predict a strong dependence on shocks, where AGN photoionization models alone fail to reproduce the observed [Si VI]/Brγ flux ratios at the 100 pc scale. Moreover, spectral analysis of the nuclear and extended X-ray emission in Fabbiano et al. (2018a) also predict shocks to be present within the central 170 pc region of ESO 428-G14 with velocities of at least a few hundred km s^{-1}. In fact, Riffel et al. (2006) report on the detection of outflows towards the North-West with velocities up to 400 km s^{-1} which they link back to the radio hotspot. This is also supported by the detection of mechanically-driven [Si VI] outflows within the boundaries of the radio emission, with velocities up to 250 km s^{-1} in the North-West and 100 km s^{-1} in the South-East (May et al. 2018).

All of the above supports the possibility that the polar dust seen in the $F1000W$ image can be driven by jet–ISM interactions. Moreover, it has been established that shocks can be a significant source of high-energy radiation (e.g. Dopita 1995; Dopita & Sutherland 1995).

Following Dopita & Sutherland (1995), the total radiative output per unit area of a shock (F_T) is given by

$$F_T = 2.28 \times 10^{-3} \left(\frac{v_s}{100\,km\,s^{-1}} \right)^{3.0} \left(\frac{n}{cm^{-3}} \right) \text{ ergs cm}^{-2}\text{s}^{-1}, \quad (3)$$

where v_s is the velocity of the shock and n is the particle number density. An important assumption here is that the post-shock gas is strongly radiative, radiating away all its thermalized energy efficiently.

Given that previous studies report high ionized gas outflow velocities associated with the NW region (~ 100 pc) from the nucleus, we adopt measurements from May et al. (2018; their table 2, region b1) for $v_s = 250$ km s^{-1} and $n = 4350$ cm^{-3}, where we have assumed that the highest ionized gas velocities are representative of the shock velocity, and that gas particle densities are equal to the electron densities measured from low-ionization gas tracers. We then compute $F_T = 156$ erg/s/cm^2. Assuming that the shocks are uniformly distributed through the region, so that their radiation can be treated as a uniform field, we can express F_T in terms of the Habing field, so that $G_0 = 653\,F_T$. Using equation (2), and taking a normal ISM grain size distribution ($a = 0.005$–0.25 μm Draine & Lee 1984), the expected temperature of the dust driven by shock heating is $T_{dust} = [154, 70]$ K.

The radiation environment arising from fast shocks in dense gas in NW2 is expected to be significantly higher than that arising from the AGN, following the reasonable values and assumptions taken in our calculations. If so, the temperatures of dust we measure in the extended emission may indeed only be possible due to the enhanced flux of higher energy photons arising from local shocks from the jet-driven outflow.

The strong enhancement of the MIR emission along the jet has been reported in other nearby AGN, notably NGC 1068 (Alloin et al. 2000) and Cygnus A (Tadhunter et al. 1990). At face value, this association of dust emission with outflows is a bit surprising, because shock models predict that dust should be destroyed by the passage of the radio jet in the high temperatures of the post-shock gas (e.g. Ferguson et al. 1997; Villar-Martín et al. 2001). However, observations show little solid evidence of dust destruction. A few possible reasons for the empirical existence of warm dust emission around radio jets were put forward by Villar-Martín et al. (2001). If the dust is confined to dense cores of gas which are resistant to the full brunt of shocks, they may survive the passage of the jet. Alternatively, the time-scale for dust destruction may be longer than the passage of the jet, or dust reformation could be efficient in the post-shock material. We also propose an additional possibility. Much of the line emission around radiative shocks is generated in gas that is ionized and illuminated by the shocks, but not directly within the post-shock gas (the so-called 'precursor' as defined by Dopita & Sutherland 1995). The dust mixed into this gas would not be destroyed by collisional processes, and can still reprocess the radiation from the shocks effectively. Therefore, if post-shock gas only occupies a modest filling factor in a jet-dominated region of the NLR, such as NW2, the dust emission we see could arise in the precursor.

Additional evidence for the role of local heating from shocks is the fact that, despite strong coronal [Si VI] emission towards the South-East NLR in ESO 428-G14, the dust continuum emission in that region is weak. The coronal lines can only be produced by the hard UV field of the AGN. Yet, despite clear AGN-ionized gas in that region, there is little warm dust. The region to the North-West, in contrast, has both coronal line emission and warm dust emission. This asymmetry is mirrored by the structure of the radio jet, which is

Table 2. The temperatures derived for the different heating models and dust grain sizes considered.

Dust Source	Grain size (μm)	Temperature (K)
Illuminated in NLR	0.005, 0.2	76, 35
From the torus	0.075, 1	44, 26
Heated by shocks	0.005, 0.2	152, 70

brighter and well-collimated only towards the North-West. We can reconcile this empirical difference by positing that a major part of the dust emission is heated directly by energy connected to the jet, such as through shocks.

If confirmed, our *JWST* observations offer a unique insight into the feedback efficiency of the jet, in both this AGN and potentially other systems that may show similar properties.

To summarize, if we assume typical ISM grains with a sizable fraction of small grains, then local shock heating is more likely to achieve the temperature of ~ 120 K that we find in the North-Western extended dust emission, at distances of 100 pc from the nucleus (see Table 2). However, this is under the idealized assumption that all the thermal energy produced in jet-driven shocks is radiated away (Dopita & Sutherland 1995), and reprocessed by dust in the vicinity of the shocks. Some of the post-shock radiation will escape the NLR, while, in turn, X-ray and hard UV heating of dust by the AGN's radiation may produce a substantial tail of warm grains. As such, heating from the central engine is also expected to contribute to the observed dust emission.

6 CONCLUSION

ESO 428-G14 shows a complex and unique NLR defined by its 'braided' strands and radio jet. In this work, we have investigated the morphology of the dust within the NLR, focusing on the inner 4 arcsec $\times$ 4 arcsec region, to provide imaging evidence of polar MIR emission, reveal its nature, and explore its origin. Our study combines *JWST*/MIRI data from the GATOS survey, using multiband imaging in five filters (*F*560*W*, *F*1000*W*, *F*1500*W*, *F*1800*W*, *F*2100*W*), with ancillary data from several facilities (ALMA, HST, SINFONI, VLA, and Spitzer) to contextualize the new MIR findings within the broader framework. Our main findings can be summarized as follows:

(i) We detect in the inner 4 arcsec $\times$ 4 arcsec region extended MIR emission in all bands, with the exception of *F*560*W* (see top panel in Fig. 2). The new MIR emission reveals an asymmetric and collimated morphology, extending along a PA of $\sim 131°$ from the North-West to the South-East, and with a total extent of ~ 450 pc (Figs 1 and 2).

(ii) We find this MIR structure to be polar, evidenced by its alignment with the radio jet and other ionized gas emission lines that define the NLR. Comparison with the ALMA CO(2-1) nuclear emission, which is a proxy for the torus orientation, reveals the MIR structure to be perpendicular to it, reinforcing its polar orientation (see Fig. 4).

(iii) We derive photometric SEDs across various regions of interest and observe that regions along the polar structure are characterized by SEDs consistent with cooler dust relative to that in disc regions. Assuming a simple blackbody, we estimate temperatures of the polar structure to be $\sim 100 - 120$ K (see regions SE1 and NW2 in Fig. 2).

(iv) We investigate emission line contamination in the *F*1000*W* image and find that the extended emission (~ 1 arcsec from the

nucleus) towards both the SE (see SE2, SE3 in Fig. 2) and NW (see NW1, NW2 in Fig. 2) regions is contaminated by [S IV], reaching a level of the order of ~ 50 per cent (see Fig. 5).

(v) We generate a pure dust continuum image from the *F*1000*W* filter and uncover that the dust is more compact, extending up to ~ 1 arcsec on each side of the nucleus. This polar dust appears to be co-spatial with the radio jet (see Fig. 6).

(vi) We explore the possible heating processes that can contribute to the polar dust reaching temperatures of ~ 120 K at $D = 100$ pc from the nucleus and predict, under the assumption of typical ISM grain size, that local heating by jet-induced shocks can reproduce similar temperatures (see Table 2). Another heating process, most likely arising from illumination through AGN radiation fields, may also be at play.

Future work on self-consistent modelling of radiative transfer through dusty NLR gas with different grain size distributions, fine tuned to the nuclear system in ESO 428-G14, will allow us to understand the origin and main heating mechanism of the extended MIR dust emission in this AGN. Moreover, while our findings indicate significant emission line contamination in ESO 428-G14, it is crucial to recognize that such contamination may not be a universal feature in all *JWST*/MIRI images. Indeed, the extent of contamination could very well be object dependent, varying depending on its specific AGN characteristics and geometry. Upcoming GATOS sample studies are poised to offer a comprehensive study of contamination.

DATA AVAILABILITY

All data used in this paper can be extracted as described in Sections 2 and 3. The reduced *JWST*/MIRI images are available online on Zenodo under the Creative Commons Attribution 4.0 International license, DOI: 10.5281/zenodo.11491161.

REFERENCES

Alloin D., Pantin E., Lagage P. O., Granato G. L., 2000, A&A, 363, 926
Alonso-Herrero A. et al., 2014, MNRAS, 443, 2766
Alonso-Herrero A. et al., 2016, MNRAS, 455, 563
Alonso-Herrero A. et al., 2018, ApJ, 859, 144
Alonso-Herrero A. et al., 2019, A&A, 628, A65
Alonso-Herrero A. et al., 2021, A&A, 652, A99
Alonso Herrero A. et al., 2023, A&A, 675, A88
Antonucci R. R. J., Miller J. S., 1985, ApJ, 297, 621
Asmus D., Hönig S. F., Gandhi P., Smette A., Duschl W. J., 2014, MNRAS, 439, 1648
Asmus D., Hönig S. F., Gandhi P., 2016, ApJ, 822, 109
Astropy Collaboration, 2013, A&A, 558, A33
Astropy Collaboration, 2018, AJ, 156, 123
Bonnet H. et al., 2004, The Messenger, 117, 17
Burtscher L., Jaffe W., Raban D., Meisenheimer K., Tristram K. R. W., Röttgering H., 2009, ApJ, 705, L53
Burtscher L. et al., 2013, A&A, 558, A149
Combes F. et al., 2019, A&A, 623, A79
Davies R. I., 2007, MNRAS, 375, 1099
Davies R. et al., 2011, ApJ, 741, 69
Dopita M. A., 1995, Ap&SS, 233, 215
Dopita M. A., Sutherland R. S., 1995, ApJ, 455, 468
Draine B. T., Lee H. M., 1984, ApJ, 285, 89
Draine B. T., Salpeter E. E., 1979, ApJ, 231, 77
Duras F. et al., 2020, A&A, 636, A73
Eisenhauer F. et al., 2003, in Iye M., Moorwood A. F. M., eds, Proc. SPIE Conf. Ser. Vol. 4841, Instrument Design and Performance for Optical/Infrared Ground-based Telescopes. SPIE, Bellingham, p. 1548
Emmering R. T., Blandford R. D., Shlosman I., 1992, ApJ, 385, 460
Fabbiano G., Elvis M., Paggi A., Karovska M., Maksym W. P., Raymond J., Risaliti G., Wang J., 2017, ApJ, 842, L4

Fabbiano G., Paggi A., Karovska M., Elvis M., Maksym W. P., Risaliti G., Wang J., 2018a, ApJ, 855, 131
Fabbiano G., Paggi A., Karovska M., Elvis M., Maksym W. P., Wang J., 2018b, ApJ, 865, 83
Fabbiano G. et al., 2019, ApJ, 870, 69
Fabian A. C., Vasudevan R. V., Gandhi P., 2008, MNRAS, 385, L43
Falcke H., Wilson A. S., Simpson C., Bower G. A., 1996, ApJ, 470, L31
Falcke H., Wilson A. S., Simpson C., 1998, ApJ, 502, 199
Ferguson J. W., Korista K. T., Ferland G. J., 1997, ApJS, 110, 287
Feruglio C., Fabbiano G., Bischetti M., Elvis M., Travascio A., Fiore F., 2020, ApJ, 890, 29
Gaia Collaboration, 2016, A&A, 595, A1
Gaia Collaboration, 2023, A&A, 674, A1
Gallimore J. F. et al., 2016, ApJ, 829, L7
Gámez Rosas V. et al., 2022, Nature, 602, 403
García-Bernete I. et al., 2015, MNRAS, 449, 1309
García-Bernete I. et al., 2016, MNRAS, 463, 3531
García-Bernete I. et al., 2022, A&A, 666, L5
García-Bernete I. et al., 2024, A&A, 681, L7
García-Burillo S. et al., 2016, ApJ, 823, L12
García-Burillo S. et al., 2019, A&A, 632, A61
García-Burillo S. et al., 2021, A&A, 652, A98
Gardner J. P. et al., 2023, PASP, 135, 068001
González-Martín O. et al., 2015, A&A, 578, A74
González-Martín O. et al., 2017, ApJ, 841, 37
González-Martín O. et al., 2019, ApJ, 884, 11
González-Martín O. et al., 2023, A&A, 676, A73
GRAVITY Collaboration, 2020, A&A, 634, A1
Harris C. R. et al., 2020, Nature, 585, 357
Hermosa Muñoz L. et al., 2024, A&A, submitted
Hönig S. F., 2019, ApJ, 884, 171
Hönig S. F., Kishimoto M., 2010, A&A, 523, A27
Hönig S. F., Kishimoto M., 2017, ApJ, 838, L20
Hönig S. F., Kishimoto M., Antonucci R., Marconi A., Prieto M. A., Tristram K., Weigelt G., 2012, ApJ, 755, 149
Hönig S. F. et al., 2013, ApJ, 771, 87
Hunter J. D., 2007, Comput. Sci. Eng., 9, 90
Isbell J. W. et al., 2022, A&A, 663, A35
Izumi T., Wada K., Fukushige R., Hamamura S., Kohno K., 2018, ApJ, 867, 48
Jaffe W. et al., 2004, Nature, 429, 47
Krolik J. H., Begelman M. C., 1988, ApJ, 329, 702
Laor A., Draine B. T., 1993, ApJ, 402, 441
Lebouteiller V., Barry D. J., Spoon H. W. W., Bernard-Salas J., Sloan G. C., Houck J. R., Weedman D. W., 2011, ApJS, 196, 8
Leftley J. H., Tristram K. R. W., Hönig S. F., Kishimoto M., Asmus D., Gandhi P., 2018, ApJ, 862, 17
Leist M. T. et al., 2024, AJ, 167, 96
Levenson N. A., Heckman T. M., Krolik J. H., Weaver K. A., Życki P. T., 2006, ApJ, 648, 111
López-Gonzaga N., Jaffe W., Burtscher L., Tristram K. R. W., Meisenheimer K., 2014, A&A, 565, A71
López-Gonzaga N., Burtscher L., Tristram K. R. W., Meisenheimer K., Schartmann M., 2016, A&A, 591, A47
Maiolino R., Salvati M., Bassani L., Dadina M., della Ceca R., Matt G., Risaliti G., Zamorani G., 1998, A&A, 338, 781
May D., Rodríguez-Ardila A., Prieto M. A., Fernández-Ontiveros J. A., Diaz Y., Mazzalay X., 2018, MNRAS, 481, L105
Nenkova M., Sirocky M. M., Ivezić Ž., Elitzur M., 2008, ApJ, 685, 147
Packham C., RADOMSkI J. T., Roche P. F., AITkEN D. K., Perlman E., Alonso-Herrero A., Colina L., Telesco C. M., 2005, ApJ, 618, L17
Pereira-Santaella M. et al., 2022, A&A, 665, L11
Perrin M. D., Sivaramakrishnan A., Lajoie C.-P., Elliott E., Pueyo L., Ravindranath S., Albert L., 2014, in Oschmann J. M. J., Clampin M., Fazio G. G., MacEwen H. A., eds, Proc. SPIE Conf. Ser. Vol. 9143, Space Telescopes and Instrumentation 2014: Optical, Infrared, and Millimeter Wave. SPIE, Bellingham, p. 91433X

Prieto M. A., Mezcua M., Fernández-Ontiveros J. A., Schartmann M., 2014, MNRAS, 442, 2145

Radomski J. T., Piña R. K., Packham C., Telesco C. M., De Buizer J. M., Fisher R. S., Robinson A., 2003, ApJ, 587, 117

Ramos Almeida C., Ricci C., 2017, Nat. Astron., 1, 679

Ramos Almeida C. et al., 2009, ApJ, 702, 1127

Ramos Almeida C. et al., 2011, ApJ, 731, 92

Reunanen J., Prieto M. A., Siebenmorgen R., 2010, MNRAS, 402, 879

Ricci C. et al., 2017, Nature, 549, 488

Rieke G. H. et al., 2015, PASP, 127, 584

Riffel R. A., Storchi-Bergmann T., Winge C., 2006, MNRAS, 373, 2

Spoon H. W. W. et al., 2022, ApJS, 259, 37

Stalevski M., Asmus D., Tristram K. R. W., 2017, MNRAS, 472, 3854

Stalevski M., Tristram K. R. W., Asmus D., 2019, MNRAS, 484, 3334

Tadhunter C. N., Scarrott S. M., Rolph C. D., 1990, MNRAS, 246, 163

Tazaki R., Ichikawa K., 2020, ApJ, 892, 149

Tielens A. G. G. M., 2010, The Physics and Chemistry of the Interstellar Medium. Cambridge Univ. Press, Cambridge

Tristram K. R. W. et al., 2007, A&A, 474, 837

Tristram K. R. W., Burtscher L., Jaffe W., Meisenheimer K., Hönig S. F., Kishimoto M., Schartmann M., Weigelt G., 2014, A&A, 563, A82

Ulvestad J. S., Wilson A. S., 1989, ApJ, 343, 659

Urry C. M., Padovani P., 1995, PASP, 107, 803

Venanzi M., Hönig S., Williamson D., 2020, ApJ, 900, 174

Véron-Cetty M. P., Véron P., 2006, A&A, 455, 773

Villar-Martín M., De Young D., Alonso-Herrero A., Allen M., Binette L., 2001, MNRAS, 328, 848

Wada K., Schartmann M., Meijerink R., 2016, ApJ, 828, L19

Williamson D., Hönig S., Venanzi M., 2020, ApJ, 897, 26

Wright G. S. et al., 2015, PASP, 127, 595

Wright G. S. et al., 2023, PASP, 135, 048003

APPENDIX A: SATURATION

The *JWST* pipeline consists of three main stages. Stage 1 performs detector level corrections, stage 2 applies flux calibrations, and finally, stage 3 combines all frames together to form one image. Our observations consist of four frames, each frame consists of 50 integrations, and each integration consists of 5 groups. By default, the first (group 1) and last group (group 5) are flagged as 'do not use' by the pipeline to avoid transient effects between exposures. As such, if saturation starts at group 3, then also groups 4 and 5 are flagged as saturated. In this case, only group 2 is flagged as good, and the pipeline fails to fit a straight line with only one point. To provide the ramp fitting with at least two good groups, we turn off the 'first frame' correction, which ordinarily flags the first group. This way, we have at least 2 groups (groups 1 and 2) to perform a linear fit, allowing us to retrieve flux measurements from these otherwise compromised pixels. While using only two groups for the ramp fitting may introduce some uncertainties in the linearity correction step due to the limited data points, this approach still provides valuable flux estimates from otherwise unusable saturated pixels.

Fig. A1 shows the X and Y intensity profiles across the nucleus in the *F*1500*W* image of ESO 428-G14, which experienced the most saturation in the nucleus. The default *JWST* pipeline results, depicted with dashed blue lines, show where this saturation occurs. We modify the pipeline by turning off the first frame correction for these pixels, thereby allowing us to gain more valid groups for the ramp fitting process (see red line). This modification ensures that at least two groups are available for a reliable fit.
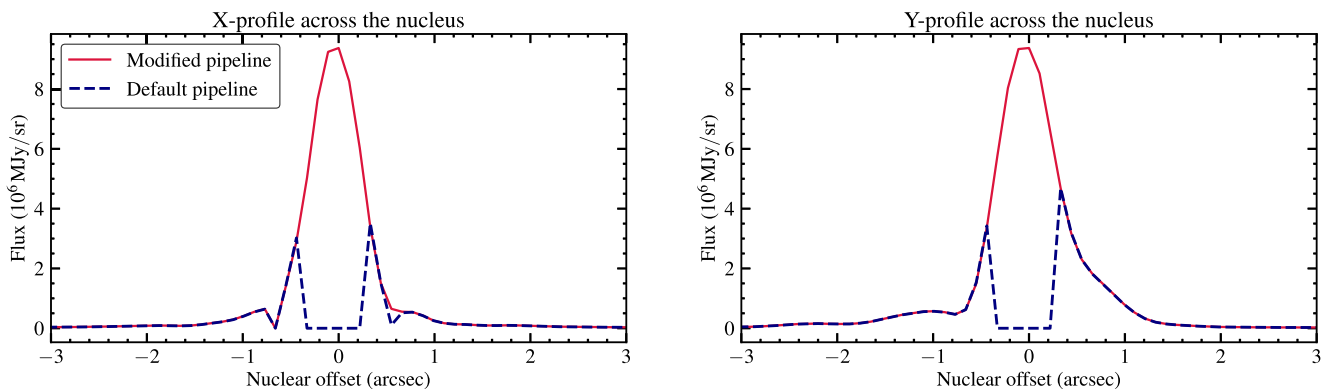
Figure A1. X and Y profiles (left-hand and right-hand panels) through the nucleus of ESO 428-G14 for the *F*15000*W* filter using the standard *JWST* pipeline, where the output image is saturated in the nucleus (see blue dashed line) compared to the modified pipeline where first frame corrections are turned off (see red line). This modified approach was adopted to gain at least two good groups for the linear ramp fitting, thereby ensuring an estimate of the flux despite the presence of other saturated groups.
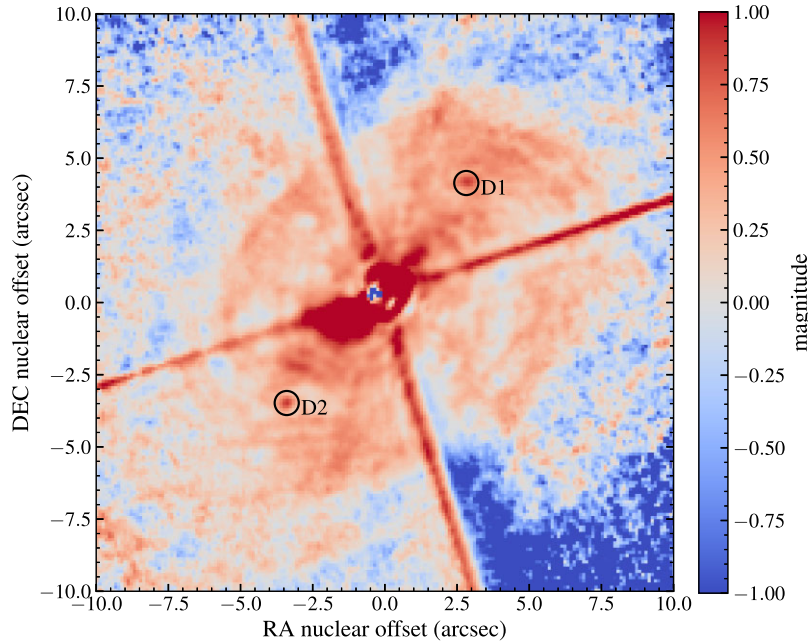
Figure B1. *F560W*– *F1000W* colour image of ESO 428-G14 expressed in units of magnitude. The circles mark the locations of D1 and D2, also identified in Fig. 3.

APPENDIX B: DISC BLOBS

Fig. B1 shows a colour image using the filters *F560W* and *F1000W*. The flux values from both images are converted to magnitudes using $M = -2.5 \log_{10}(F)$, where F is flux. The image is colour coded such that red indicates redder (cooler) magnitudes, while blue indicates bluer (hotter) temperatures. This highlights the SF disc regions D1 (in the North-West) and D2 (in the South-East) presented in Fig. 3, making them stand out against the disc. Interestingly, D1 and D2 are along a similar PA to the extended polar dust. This alignment hints to the contribution of AGN activity in their heating. Recent paper by Hermosa Muñoz (2024, submitted) reports on the detection of SF knots along the direction of the outflow in NGC 7172. Future kinematic analysis of ESO 428-G14 would allow us to shed light on to the nature of these regions.

[1]*School of Mathematics, Statistics and Physics, Newcastle University, Newcastle upon Tyne NE1 7RU, UK*

[2]*Centro de Astrobiología (CAB), CSIC-INTA, Camino Bajo del Castillo s/n, Villanueva de la Cañada, E-28692 Madrid, Spain*

[3]*Instituto de Física Fundamental, CSIC, Calle Serrano 123, E-28006 Madrid, Spain*

[4]*Department of Physics, University of Oxford, Keble Road, Oxford OX1 3RH, UK*

[5]*Department of Physics & Astronomy, University of Southampton, Highfield, Southampton SO171BJ, UK*

[6]*Instituto de Astrofísica de Canarias, Calle Vía Láctea, s/n, E-38205 La Laguna, Tenerife, Spain*

[7]*Departamento de Astrofísica, Universidad de La Laguna, E-38206 La Laguna, Tenerife, Spain*

[8]*Department of Physics & Astronomy, University of Alaska Anchorage, Anchorage, AK 99508-4664, USA*

[9]*Department of Physics, University of Alaska, Fairbanks, AK 99775-5920, USA*

[10]*Department of Physics and Astronomy, The University of Texas at San Antonio, 1 UTSA Circle, San Antonio, TX 78249-0600, USA*

[11]*Max Planck Institute for Extraterrestrial Physics (MPE), Giessenbachstr 1, D-85748 Garching, Germany*

[12]*Instituto de Estudios Astrofísicos, Facultad de Ingeniería y Ciencias, Universidad Diego Portales, Av. Ejército Libertador 441, Santiago, Chile*

[13]*Kavli Institute for Astronomy and Astrophysics, Peking University, Beijing 100871, China*

[14]*Kavli Institute for Particle Astrophysics & Cosmology (KIPAC), Stanford University, Stanford, CA 94305, USA*

[15]*Observatorio Astronómico Nacional (OAN-IGN)-Observatorio de Madrid, Alfonso XII, 3, E-28014 Madrid, Spain*

[16]*National Astronomical Observatory of Japan, National Institutes of Natural Sciences (NINS), 2-21-1 Osawa, Mitaka, Tokyo 181-8588, Japan*

[17]*Departmento de Física de la Tierra y Astrofísica, Fac. de CC Físicas, Universidad Complutense de Madrid, E-28040 Madrid, Spain*

[18]*Instituto de Física de Partículas y del Cosmos IPARCOS, Fac. CC Físicas, Universidad Complutense de Madrid, E-28040 Madrid, Spain*

[19]*Cahill Center for Astrophysics, California Institute of Technology, 1216 East California Boulevard, Pasadena, CA 91125, USA*

[20]*Astronomical Institute, Academy of Sciences, Boční II 1401, CZ-14131 Prague, Czech Republic*

[21]*LERMA, Observatoire de Paris, Collège de France, PSL University, CNRS, Sorbonne University, F-75014 Paris, France*

[22]*Institute of Astrophysics, Foundation for Research and Technology-Hellas (FORTH), Heraklion, GR-70013, Greece*

[23]*School of Sciences, European University Cyprus, Diogenes street, Engomi, 1516 Nicosia, Cyprus*

[24]*Instituto de Radioastronomía y Astrofísica (IRyA), Universidad Nacional Autónoma de México, Antigua Carretera a Pátzcuaro #8701, Colonia ExHda. San José de la Huerta, Morelia, Michoacán, México C.P. 58089, México*

[25]*Telespazio UK for ESA, ESAC, Camino Bajo del Castillo s/n, E-28692 Villanueva de la Cañada, Spain*

[26]*Space Telescope Science Institute, 3700 San Martin Drive, Baltimore, MD 21218, USA*

[27]*Gemini Observatory/NSF's NOIRLab, Casilla 603, La Serena, Chile*

[28] *School of Sciences, European University Cyprus, Diogenes street, Engomi, 1516 Nicosia, Cyprus*
[29] *Laboratório Nacional de Astrofísica/MCTI, 37530-000 Itajubá, MG, Brazil*
[30] *Observatório Nacional, Rua General José Cristino, 77, 20921-400 São Cristóvão, Rio de Janeiro, RJ, Brazil*
[31] *Astronomical Observatory, Volgina 7, 11060 Belgrade, Serbia*

[32] *Sterrenkundig Observatorium, Universiteit Gent, Krijgslaan 281-S9, Gent B-9000, Belgium*
[33] *Centre for Extragalactic Astronomy, Department of Physics, Durham University, South Road, Durham DH1 3LE, UK*

This paper has been typeset from a TEX/LATEX file prepared by the author.